TOGGLE identifies fate and function process within a single type of mature cell through single-cell transcriptomics.

Junpeng Chen[1,2,17+], Eric Jiang[3+], Zhouweiyu Chen[4+], Kaiqing Liu[1,2+], Tianda Sun[5], Yibing Nong[1], Yunhui Kong[6], Tao Yuan[9], Pawan Daga[10], Charles C. Dai[11,12], Yexing Yan[14], Jinwen Ge[7,8], Haihui Wu[15], Tong Yang[7], Shanshan Wang[7], Zixiang Su[16], Changping Li*, You Li[3]*, Kailin Yang[7,8]*, Richa A. Singhal[17]*, Lu Cai[2*], Alex P. Carll[1,17]*

1, Department of Physiology, University of Louisville School of Medicine, Louisville, Kentucky,40204, USA

2, Pediatric Research Institute, Department of Pediatrics, University of Louisville School of Medicine, Louisville, Kentucky 40202, USA

3, Kebei Hospital of Shaoxing, Shaoxing City 312081, China

4 Address: Xiangtan University, Xiangtan 411105, China

5 Address: Department of Computer Science, University of York, Heslington, York YO10 5DD, United Kingdom

6 Address: Institute of Modern Biology, Nanjing University, NanJing, 210008, China, kongyunhui1@gmail.com

7 Address: Key Laboratory of Hunan Province for Integrated Traditional Chinese and Western Medicine on Prevention and Treatment of Cardio-Cerebral Diseases, School of Integrated Chinese and Western Medicine, Hunan University of Chinese Medicine, Changsha, China

8 Address: Hunan Academy of Chinese Medicine, Changsha, China

9 Address: College of Mechanical Engineering and Automation, Huaqiao University, Xianmen, China, yuan__t@163.com

10 Address: Department of Internal Medicine, University of Louisville, Kentucky, USA

11 Address: Department of Oral and Maxillofacial Surgery, School of Dentistry, University of Maryland, Baltimore, Maryland 21201, USA.

12 Address: Fischell Department of Bioengineering, A. James Clark School of Engineering, University of Maryland, College Park, Maryland 20742, USA

13 Address: School of mechanical engineering and automation, Fuyao University of Science and Technology, Fuzhou, China

14 Address: Pinghu Hospital of Traditional Chinese Medicine, Pinghu, Zhejiang Province, China

15 Address: Department of Psychology, Daqing Hospital of Traditional Chinese Medicine, Daqing, China

16 Address: University of Minnesota, College of Biological Sciences, St. Paul, MN 55108, USA, suzixiang.mitchell@gmail.com

17 Address: Center for Cardiometabolic Science, Division of Environmental Medicine, Christina Lee Brown Envirome Insttitute, University of Louisville, Louisville, KY 40202, United States.

+ Junpeng Chen (drchenjunpeng@hotmail.com), Eric Jiang (jyjiang@link.cuhk.edu.hk), Zhouweiyu Chen (yahoo_con_cn@163.com) and Kaiqing Liu are co-first authors who have contributed an indispensable part to this article and should be considered to have made equal contributions. Their names are listed without any specific order.

*Corresponding author should be: Changping Li, You Li (liyou@cjgs23.wecom.work), Kailin Yang (yklab2014@hotmail.com),Alex P. Carll (Alex.Carll@louisville.edu). Alex P. Carll is the project and Lab leader.

Abstract

Almost inevitably, mature cells meet their demise through specific processes of phenotypic change such as apoptosis. Although single-cell RNA sequencing (scRNA-seq) technology can reconstruct processes like life cycles and disease progression, identifying specific types of cell death in dying cells remains challenging due to the complexity of related signaling pathways and marker genes. To address this, our study introduces a fate prediction method, TOGGLE, which reconstructs complete programmed cell fates from untracked data. Based on a corollary of Takens' theorem, TOGGLE enables analysis of highly similar programmed cell death data with indistinct fate boundaries. This approach circumvents the need for live sample tracking and serial assessments. In hematopoiesis and reprogramming, TOGGLE reconstructs full fate biases and predicts cell differentiation from early development to maturity. In brain tissue from a murine model of cerebral infarction, TOGGLE predicts the fate trajectories of neurons undergoing post-infarction programmed cell death (especially ferroptosis) and identifies genes expressed differentially between dying and healthy neurons. Subsequently, functional transitions and differences were discussed using cells from the heart.

1 Introduction

The phenotype of terminally differentiated cells inevitably morphs toward one of many pathways of cell death. Whole tissues may bear cells following distinct molecular patterns that dictate separate fates; for example, upon cerebral infarction, neurons in ischemic stroke may succumb to to programmed cell death such as ferroptosis, apoptosis or pyroptosis, at different stages of pathogenesis and under different conditions[1–4]. Given the complexity of signaling pathways and marker genes involved in programmed cell death, identifying the specific type of cell death occurring in cells remains challenging. Ferroptosis poses a powerful example of the value for distinguishing between types of programmed cell death. As a crucial form of programmed cell death in mature cells, ferroptosis is involved not only in embryonic development but also in tumor growth, immune evasion, and muscle atrophy, and catalyzed by iron [5–8]. In ischemic stroke (cerebral infarction), a cerebrovascular disease with high rates of mortality and disability, ferroptosis significantly contributes to neuronal death [9,10]. Regulating ferroptosis is essential for rescuing dying neurons and restoring the function of at-risk neurons in affected brain areas[9,10]. Despite the importance of ferroptosis, its mechanisms remain poorly understood[7]. With advancements in technology, single-cell RNA sequencing (scRNA-seq) has become a valuable tool for studying ferroptosis in brain cells during ischemic stroke. However, due to limitations in analytical methods, most

research has focused on neuroglia cells[11,12], with only a few using scRNA-seq to study neurons[13]. In the few studies that have analyzed scRNA-seq data from neurons, existing tools can identify neuron types (e.g.,glutamatergic neurons)[13] but cannot distinguish between different neuronal states, including whether they are undergoing necrosis or their stage of programmed cell death. Characterizing the contributions of different modes of cell death across neuronal cell populations after cerebral infarction could facilitate the development of new therapies. Indeed, in virtually any model of tissue injury, a fate-prediction tool that leverages scRNA-seq data to map trajectories of programmed cell death, differentiate cells undergoing programmed death from those undergoing alternate processes, and specify type of programmed death for each cell would elucidate the types of programmed death that mediate disease progression and potentially open new avenues for therapeutic development. This is not merely a prediction process; it should enable the distinction of stages in mature cells.

While there are numerous tools available for analyzing scRNA-seq data, few are designed to predict the fate of Mature cells, such as neurons. Current computational methods include Weighted Optimal Transport (WOT)[14] and Cospar[15]. WOT constructs lineage information based on dynamic data trajectories but tends to misidentify similar transition trajectories. Cospar utilizes transition matrix principles to infer state transitions between nodes. However, it is not suitable for multi-stage classifications where correspondences are not unique; it cannot classify static, differentiated cell data, such as Mature cells, nor can it distinguish between different programmed stages within the same cell type. The primary challenges in fate prediction, illustrated in **Figure 1**.

Figure 1. Challenges in Cell Fate prediction.

2 Results

We used hematopoietic and fibroblast reprogramming datasets to reconstruct cell lineages. TOGGLE successfully identified progenitor cells from the entire dataset, demonstrating its capability to classify functionally continuous cells into distinct types. Furthermore, TOGGLE predicted the developmental trajectory of progenitor cells, indicating its ability to perform intra-class classification within the same cell type. Previous algorithms were used for subtype classification of cells or binary classification of differentiation in developing cells, which required extensive preprocessing. However, TOGGLE can directly distinguish between progenitor cells, what do progenitor cells develop into, and differentiated cells, thereby eliminating the need for cumbersome identification and preprocessing steps.

Programmed cell fate is driven by RNA transcriptional pathways, and some studies focus on how these pathways are transformed. For example, with the increasing attention on RNA pathway alterations among public health specialists, we utilized datasets on e-cigarette and nicotine exposures to analyze changes in cellular RNA pathways, These changes are not caused by genetic factors and may reflect the influence of non-epigenetic factors and long-term metabolic changes. The same computational process was applied to the differential genes in these datasets. Through long-term alterations in RNA pathways, cells may ultimately change their function. Therefore, identifying cell fate also requires distinguishing the execution of cellular functions as a crucial step.

Subsequently, we used neurons undergoing ferroptosis as sample to establish the programmed fate lineage of mature cells. Following ischemic stroke, cells within ischemic areas generally undergo various forms of programmed cell death, including apoptosis, autophagy, pyroptosis, and ferroptosis[16–18]. Conventional single-cell sequencing analysis tools face limitations in examining these multifaceted, progressive neuronal death processes. This is due to the challenge of capturing data from neurons that have already died, and because programmed cell death lacks a clear "decision boundary," making the construction of fate trajectories complex. Previous studies focused on cell subtype classification and cell type classification. Building on this foundation, TOGGLE can further distinguish different functional states within the same cell subtype, as well as differentiate the programmed fate stages within the same cell subtype.

A functional comparison table is provided in the Discussion.

2.1 Trace the cell lineage of hematopoietic development

To assess the efficacy of TOGGLE and make comparisons with other methods, we applied it to publicly available datasets with known lineage obtained from the Cospar software. The first dataset traced the differentiation of mouse bone marrow hematopoietic progenitor cells (HPCs) in a controlled culture environment over four timepoints[9]. We identified cells using the method in Weinreb et al.'s work[9] and focused our analysis on three cell types: progenitor cells, monocytes, and neutrophils: progenitor cells, monocytes, and neutrophils. Progenitor cells exhibit a dual fate bias, as defined in the original Cospar research paper[15], where a portion differentiates into monocytes (referred to as monocyte progenitors), while another portion differentiates into neutrophils (referred to as neutrophil progenitors)[10]. Our objective is to trace the fate bias of progenitor cells, specifically to identify monocyte progenitors and neutrophil progenitors within the progenitor cell population.

TOGGLE is an unsupervised method. TOGGLE first generates a similarity matrix described by graph distances(Chapter 4.2). Cells that are relatively close are considered to have the same fate preferences and are clustered into a unified group in the same iteration round. The algorithm segments

the distance matrix through binarization(Chapter 4.3), initially obtaining a boundary, then iteratively generating a second boundary based on the first(Chapter 4.4). Each classification results in a positively correlated group and a negatively correlated group, with the boundary between them forming a dividing line. Within the positively correlated group, a secondary positively correlated group and a secondary negatively correlated group are identified. Similarly, within the negatively correlated group, a secondary positively correlated group and a secondary negatively correlated group are identified. This process creates a total of two new boundaries at the intersections(Chapter 4.4). This process results in different groupings of cells, which are then sorted. After sorting, then deriving the required number of categorie according to the resolution set by number of target categories boundaries(Chapter 4.5). After completing the segmentation, samples within adjacent boundaries form a cluster. In this process, progenitor cells close to neutrophils are determined by TOGGLE to be neutrophil progenitors, while progenitor cells close to monocytes are determined to be monocyte progenitors (Figure 2G). (1)When analyzing descendants independently, by comparing with the true tracing labels in ground truth analysis, the accuracy of TOGGLE is found to be 77%, predict result as Figure 2H. Notably, the TOGGLE algorithm is implemented as a unsupervised method without prior training. In order to evaluate the performance of TOGGLE, we compared it to four widely used in silico algorithms: Cospar, Super OT, WOT, and GAN-Based OT. Cospar attained a rate of 65%, Super OT exhibited a slightly higher accuracy at 67%, WOT maintained a similar accuracy of 65%, and GAN-Based OT achieved 62%. (2)When both progenitor and descendant cells are selected for classification, TOGGLE achieves an accuracy of 82%. The accuracy of WOT is less than 50%, while Cospar cannot be used for this calculation.

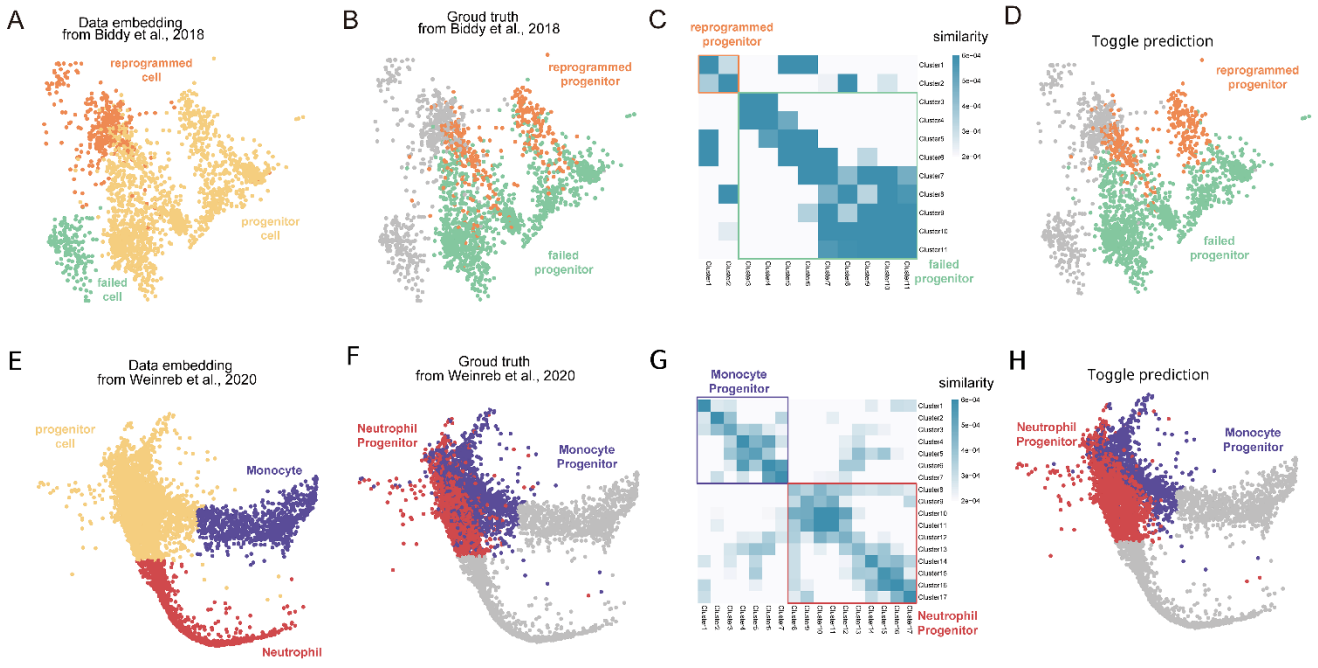

Figure 2. Tracing the lineage of fibroblast reprogramming[9] and hematopoietic cell[16] development. A: Data embedding of scRNA-seq data on experimentally-induced fibroblast reprogramming over six sampled timepoints in Biddy et al., 2018[19]; B: Ground truth of reprogrammed data; C: Similarity matrix of clustering results of reprogrammed data; D: TOGGLE's prediction result of reprogrammed data; E: Data embedding of neutrophil progenitor data from Weinreb et al. 2020[9]; F: Ground truth of neutrophil progenitor data; G: The similarity matrix of clustering results of neutrophil progenitor data; H: The TOGGLE's prediction result of neutrophil progenitor data.

2.2 Trace the cell lineage of fibroblast reprogramming

We also validated the performance of TOGGLE on a dataset from mouse embryonic fibroblasts sampled at eight timepoints across transcription factor (TF) direct lineage reprogramming to induced endoderm progenitor cells. In this experiment, cells initially expanded, but many were lost due to aging or cell death. By day 28, 30% of the cells were successfully reprogrammed[19]. Building on the work of Biddy et al.[19], we identified cells using genes such as *Spint2, Apoa1, Peg3, and Col1a2*, which are strongly correlated with successful or failed reprogramming. For further analysis, we focused on progenitor cells (fibroblasts), reprogrammed cells, and failed cells. Induced progenitor cells display a dual fate bias, wherein a fraction differentiates into reprogrammed cells, referred to as reprogrammed progenitors, while another fraction differentiates into failed-reprogrammed cells, referred to as failed progenitors[19]. Here, we investigated the fate bias of fibroblasts undergoing transcription factor-induced reprogramming to progenitors, specifically by identifying the successfully reprogrammed progenitors and failed progenitors within the progenitor cell population.

We employed TOGGLE to reconstruct the complete tracing of the reprogramming process of fibroblasts to stem cells, methods same as chapter 2.1. After completing the segmentation, samples within adjacent boundaries form a cluster. In this process, progenitor cells close to Reprogrammed cells are identified by TOGGLE as Reprogrammed progenitor cells, while those close to Failed cells are identified as Failed progenitor cells (Figure 2C). (1)When analyzing descendants independently, by comparing with the true tracing labels in the ground truth, TOGGLE achieved an accuracy of 91.32%, predict result as Figure 2D. TOGGLE is a unsupervised algorithm, and we benchmarked it against the two most common in silico algorithms, with Cospar's accuracy being 67%, and WOT's accuracy being 31%, showing a significant accuracy advantage. (2)When both progenitor and descendant cells are selected for classification, TOGGLE achieves an accuracy of 84%. The accuracy of WOT is less than 50%, while Cospar cannot be used for this calculation.

2.3 Fate Differentiation of Mature Cells

2.3.1 Changes in RNA Pathways

TOGGLE was applied to analyze the effects of e-cigarette aerosol inhalation on mouse cardiac tissue using dataset. Taking the differentially expressed genes of adult mice exposed to e-cigarette smoke and fresh air as an example, they were divided into 6 groups(Chapter 4.5). Except for Group 2, Group 3, Group 4 and Group 5, the remaining groups did not show significant enrichment in biological processes or KEGG signaling pathways and require further investigation (Figure 3). The enrichment results of each gene group and the grouping results of differentially expressed genes for other intervention methods are shown in Supplementary Material 7. The results indicate that exposure to e-cigarette aerosol significantly altered RNA pathways in the hearts of mice. These changes are reflected in the grouping of differentially expressed genes and their enrichment in biological functions and signaling pathways. More pronounced immune and inflammatory responses (e.g., TNF signaling) and cell cycle-related changes among young mice compared to mature adults suggested that the impact of e-cigarette use is greater at younger ages.

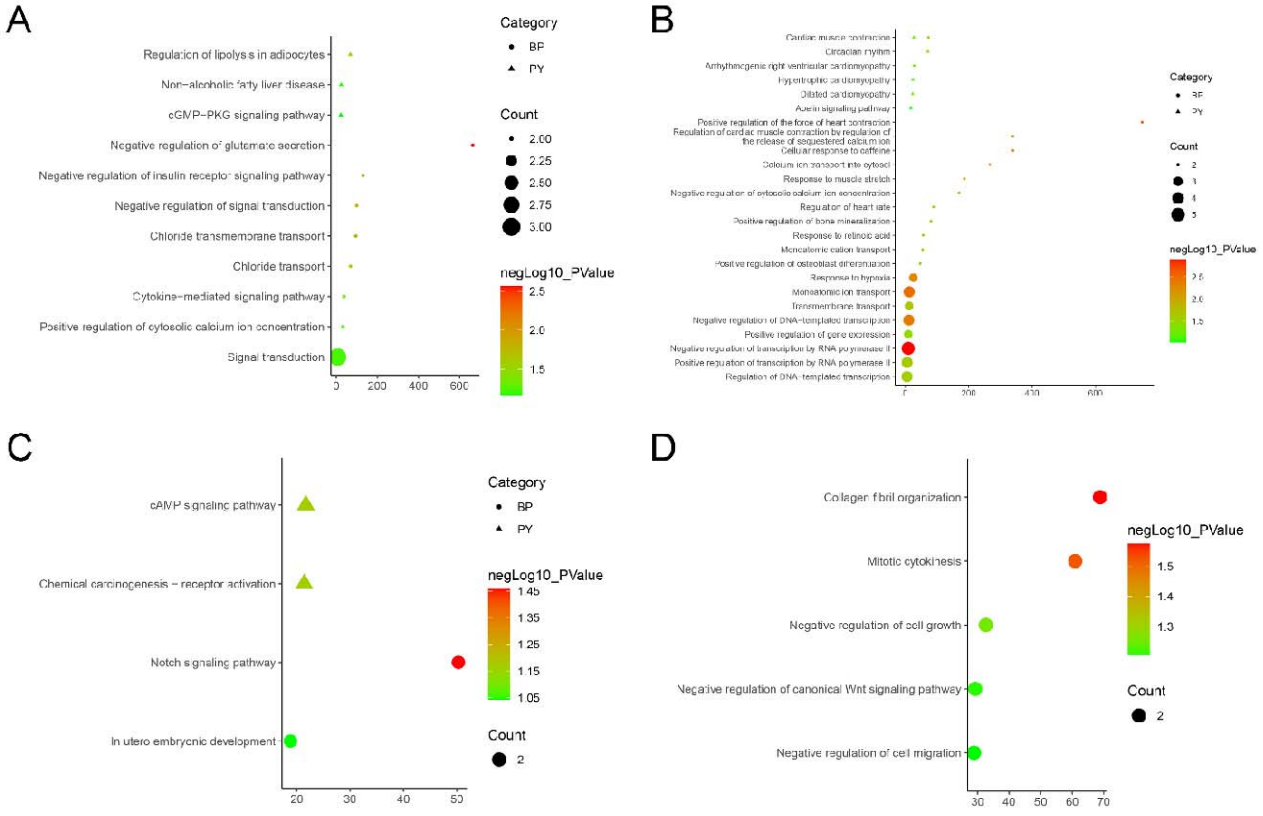

Figure 3. The Enrichment Results of Genes in Each Gene Group. A: Biological processes and pathways of Group 2; B: Biological processes and pathways of Group 3; C: Biological processes and pathways of Group 4; D: Biological processes of Group 5. (BP: biological processes; PY: signaling pathways. X-axis is fold enrichment)

2.3.2 Functional Differentiation of Mature Cells

TOGGLE was applied to analyze single-nucleus RNA sequencing (snRNA-seq) and bulk RNA sequencing (bulk-RNA seq) data from a rat myocardial infarction (MI) model. After classifying the snRNA-seq data into various cell types, including fibroblasts, myofibroblasts, macrophages, T cells, and cardiomyocytes (Figure 4A), TOGGLE divided the fibroblasts and myofibroblasts into seven groups (Figure 4B). The MI group was predominantly represented by FibR1-G5, FibR1-G6, and FibR1-G7 (Figure 4C). The results of the inferred ligand-receptor interactions between these fibroblasts and T cells or macrophages (cell-cell communication) revealed differences in the strength and types of interactions, suggesting functional variations among these fibroblast subgroups (Figures 4D and 4E). Further analysis of the highly variable genes in the MI fibroblasts also identified eight distinct functional groups (Figure 4F). Additionally, TOGGLE was used to map bulk RNA-seq data onto the snRNA-seq dataset, revealing that the gene expression pattern of fibroblasts in the bulk RNA-seq MI group closely matched that of FibR2-G6 (highlighted in the red box in Figure 4G). This finding suggests that the bulk RNA-seq fibroblasts predominantly exhibit functions similar to those of FibR2-G6, which are associated with cell migration, adhesion, angiogenesis, and ECM-receptor interactions (Figure 4H).

Thus, TOGGLE can effectively combine bulk RNA-seq data with snRNA-seq to contextualize each, and which cell types and specific phenotypes undergo nuclear transcriptional changes that most closely represent overall tissue-level changes in transcription.

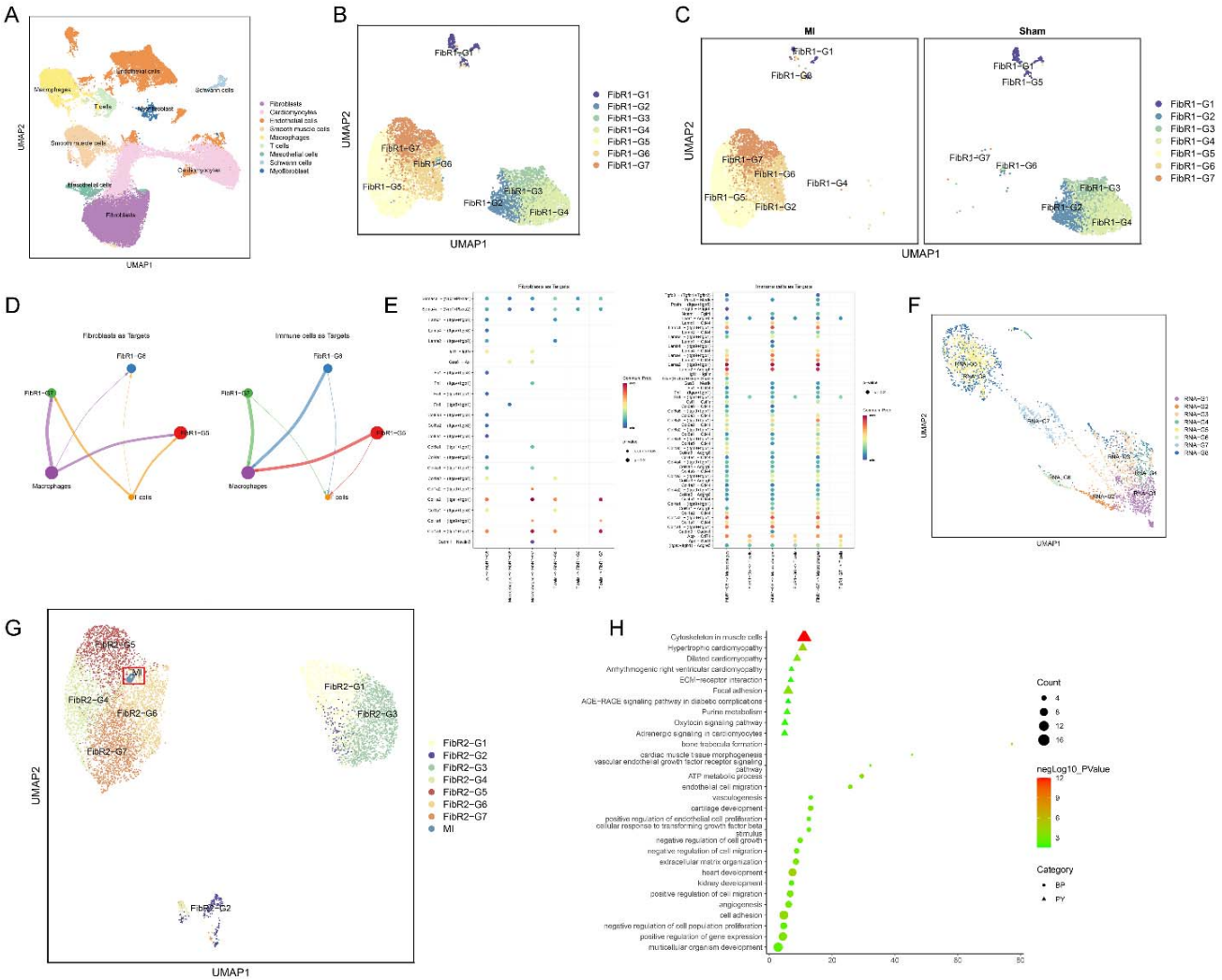

Figure 4 Analysis results of set. A: Cell types of snRNA-seq; B: Fibroblasts and myofibroblasts were divided into 7 groups after TOGGLE analysis; C: Distribution of 7 cell types in MI cohort and Sham cohort; D: Weight/strength diagram of cell communication between fibroblasts and immune cells; E: Bubble diagram of cell communication between fibroblasts and immune cells; F: RNA distribution of fibroblasts in the MI group; G: Mapping MI group bulk RNA-seq data onto UMAP of fibroblast snRNA-seq results; H: Enrichment results of FibR2-G6 (BP: biological processes; PY: signaling pathways. X-axis is fold enrichment).

2.4 Programmed Cell Death Trajectories Prediction in Neurons

2.4.1 Preliminary Prediction of Ischemic Stroke-Induced Neuronal Fate

The above results confirm the reliability of TOGGLE for predicting cell fate. In cases of ischemic stroke, neurons often undergo programmed cell death, with ferroptosis playing a significant role in neuronal loss. However, ferroptosis frequently overlaps with other forms of programmed cell death,

making it challenging for existing algorithms to effectively distinguish ferroptosis from other cell death mechanisms. Therefore, we applied TOGGLE to predict and analyze neuronal fate in a rat model of ischemic stroke, distinguishing between healthy and dying neurons to forecast programmed cell death, particularly ferroptosis. And we further verified the expression of apoptosis genes and ferroptosis genes in animal experiments. Ischemic stroke samples [middle cerebral artery occlusion (MCAO) cohort] and healthy samples (Sham cohort) from the were included in the analysis[13]. The neuronal scRNA-seq data were then analyzed using TOGGLE and initially divided into five groups by dimension reduction using UMAP: Group R1-1, Group R1-2, Group R1-3, Group R1-4, and Group R1-5 (Figure 5A).

Cohorts were analyzed for differentially expressed genes, which we cross-referenced with programmed cell death-related genes[3] that we then counted in each comparison group (Figure 3D). Group R1-1 vs. Group R1-5 had fewer programmed cell death-related genes, while comparisons between Group R1-1 and other groups, as well as Group R1-5 and other groups, had a higher number of programmed cell death-related genes. This suggests that Group R1-1 and Group R1-5 exhibit similar states, potentially representing consecutive stages in a continuum. Additionally, the cell counts of Group R1-1 and Group R1-5 in the sham cohort were high (Figure 5B and 5C), suggesting that both groups consisted of cells that had not entered a programmed cell death state. Given that Group R1-5 was abundant in both MCAO cohort and sham cohort, we inferred that it represented healthy cells. Furthermore, Group R1-2 cells were more prevalent in the MCAO cohort compared to sham and had a significantly more differentially expressed programmed cell death-related genes compared to other cell groups, indicating that Group R1-2 consists of cells that have entered a programmed cell death state. Given the moderate number of differentially expressed programmed cell death-related genes among cells in Group R1-3 and Group R1-4, they are inferred to be in intermediate states.

Based on CellMarker, the cells of Group R1-3 were identified as Mtss2+Gpr37l1+ glutamatergic neurons, and that of Group R1-4 were identified as Atp2b2+Grin2a+ glutamatergic neurons. As shown in Figure 5B and 3C, the cell counts of Group R1-3 and Group R1-4 showed little difference between the MCAO and Sham cohorts, which suggests that these two groups of cells had not undergone programmed cell death. Therefore, these groups were excluded from further analysis. The UMAP plots after excluding Groups R1-3 and R1-4 are shown in Figure 5E.

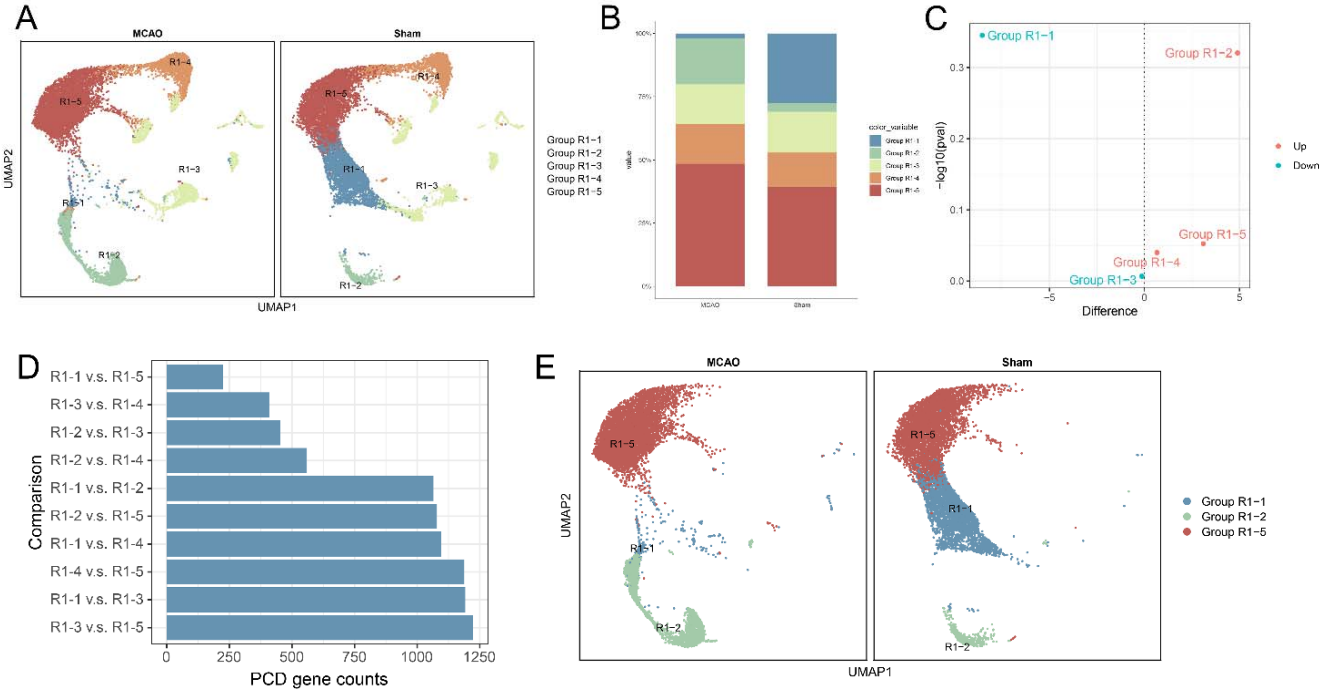

Figure 5. Preliminary Prediction of Neuronal Fate. A: The grouping results of the preliminary analysis; B: The proportion of each cell group in MCAO and Sham; C: Compared with Sham cohort, the changes in cell number in each cell group in MCAO cohort; D: Comparison of the number of differentially expressed programmed cell death genes between cell groups of all cohorts; E: UMAP graph without R1-3 and R1-4.

2.4.2 Prediction of Neuronal Programmed Cell Death Trajectories

The data of Group R1-1, Group R1-2, and Group R1-5 of the preliminary analysis results were further analyzed to predict their programmed cell death trajectories. Monocle3 was utilized to analyze their pseudotime (Figure 6A), it can be observed that the loss of temporal information is significant because the time restoration is not synchronized with the trajectory scale. And based on this data, TOGGLE identified 9 subgroups (Figure 6B and 6C). Based on the number of programmed cell death-related genes and the cell count within each group (Figure 6D), the following can be inferred: (1) Groups R2-1 are closely related to Group R2-6. (2) Groups R2-3 are distant from Groups R2-5, R2-6, and R2-7; similarly, Groups R2-1 are distant from Groups R2-5 and R2-7, consistent with the pseudotime analysis. (3) Group R2-2 is closely related to Group R2-4; however, since the cell counts of Group R2-2 in the sham cohort is larger, it is considered potential noise (Figure 6E, 6F, 6G). R2-9 cells are likely representative of healthy cells. R2-8 cells are predominantly observed in the MCAO cohort, while R2-1, R2-5, R2-6, and R2-7 are more frequent in the Sham cohort, suggesting they may represent intermediate states transitioning toward programmed cell death. In contrast, R2-2 and R2-3 cells show a marked increase in the MCAO cohort, indicating they are primarily composed of cells undergoing

programmed cell death. The trajectory of programmed cell death may be Group R2-9→Group R2-8→Group R2-1→Groups R2-5 to R2-7→Group R2-2→Group R2-3.

In summary, we deduced that Group R2-9 is the most likely starting point and Group R2-3 the most plausible terminus. The FindMarkers function of Seurat was used to perform precise differential gene expression analysis. Group R2-1, Group R2-2, Group R2-3, Groups R2-5 to R2-7, and Group R2-8 were set as ident1, and Group R2-9 was set as ident2. The volcano plot of Group R2-9 v.s. Group R2-3 genes is shown in Figure 6H. The differentially expressed genes between these groups were imported into DAVID (ver. 2024q2, https://david.ncifcrf.gov) for Kyoto Encyclopedia of Genes and Genomes (KEGG) signaling pathway enrichment analysis, so as to obtain the number of genes in representative programmed cell death pathways (such as apoptosis and ferroptosis) (Figure 6I and 6J). It was found that as the trajectory moved away from Group R2-9, the number of apoptosis- and ferroptosis-related genes expressed in each group gradually increased, which was consistent with the inferred time trajectory. The results of enrichment analysis are shown in Table S1 (see supplementary materials), and the differentially expressed genes are shown in Table S2.

Among the differentially expressed genes of Group R2-3 vs. Group R2-9 (Table S2), several apoptosis- and ferroptosis-related genes were identified: *Gpx4* (Log2FC=-0.60, FDR<0.05), *Trf* (Log2FC=6.98, FDR<0.05), *Tfrc* (also known as *TFR*, Log2FC=3.38, FDR<0.05), *Smad1* (Log2FC=1.16, FDR<0.05), *Smad5* (Log2FC=1.70, FDR<0.05), *Acsl4* (Log2FC=1.39, FDR<0.05), *Rela* (also known as *p65*, Log2FC=1.08, FDR<0.05), *Bax* (Log2FC=1.46, FDR<0.05), and *Nfkbia* (also known as *IkBA*, Log2FC=4.00, FDR<0.05). These gene expression patterns are consistent with those observed during apoptosis and ferroptosis. However, several apoptosis- and ferroptosis-related genes showed expressions inconsistent with previous studies, including *Aifm2* (also known as *FSP1*, Log2FC=0.66, FDR<0.05), *Sirt1* (Log2FC=2.56, FDR<0.05), and *Casp3* (Log2FC=-0.40, FDR<0.05). This may be because cells in the early stages of programmed cell death are trying to "self-rescue." In addition, some positively expressed ferroptosis-driving genes were found in the differentially expressed genes. The ferroptosis-driving genes refer to FerrDb V2 (http://www.zhounan.org/ferrdb/current/)[21] (Table S2). The positions of these genes within relevant pathways are illustrated in Figure 7.

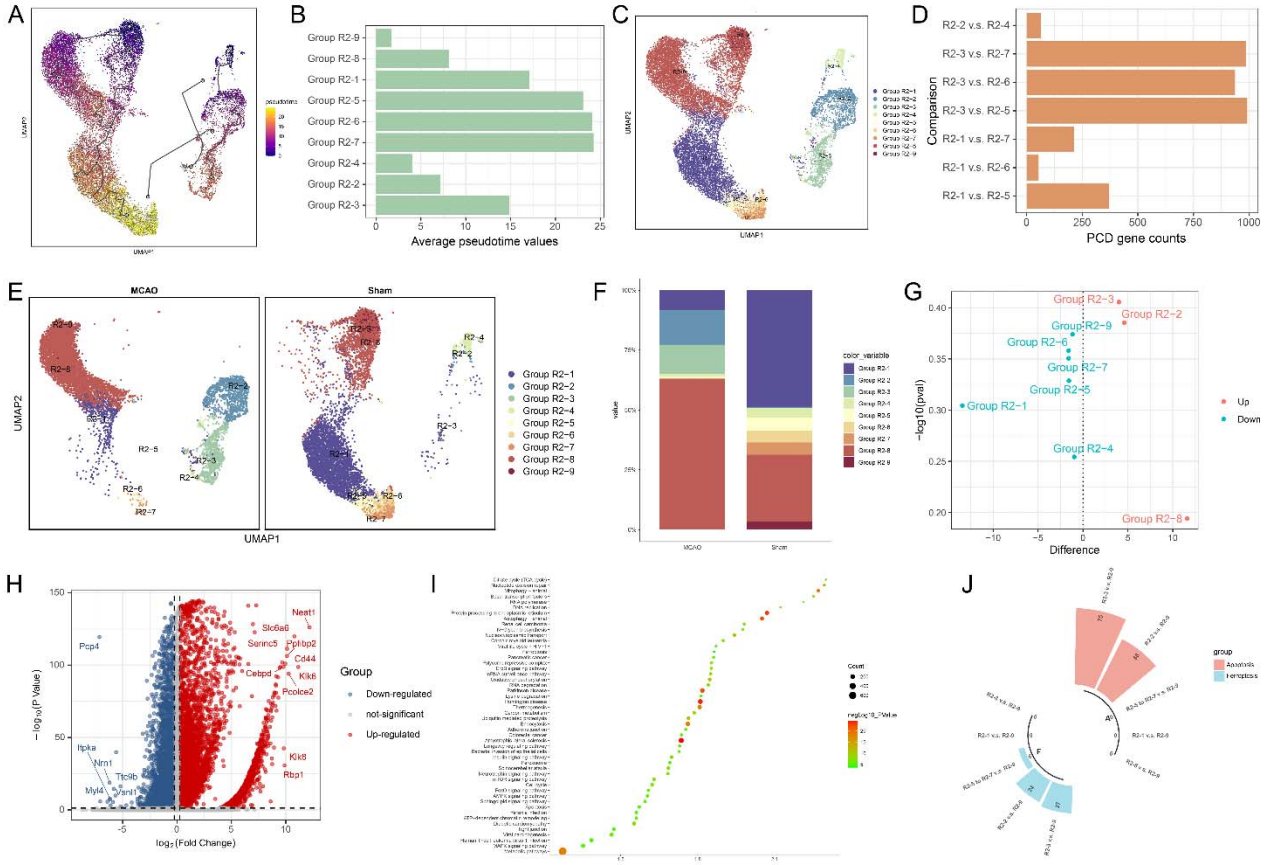

Figure 6. Programmed Cell Death Trajectories Prediction. A: Pseudo-time trajectory of cells; B: The average pseudotime values of groups; C: Cells in previous groups R1-1, R1-2, R1-5 further analyzed by TOGGLE that divided into 9 groups; D: The number of programmed cell death genes in each cell group; E: Distribution of cell groups in Sham and MCAO; F: The proportion of those 9 cell groups in MCAO and Sham; G: Compared with Sham, the changes in cell number in those 9 cell groups in MCAO; H: Volcano plot of Group R2-3 v.s. Group R2-9 genes; I: Top 50 pathways of Group R2-3 v.s. Group R2-9 genes; J: The number of genes enriched in apoptosis and ferroptosis. Pink genes were selected for experimental verification in follow-up studies (Figure 9 and Figure 10). PCD: programmed cell death.

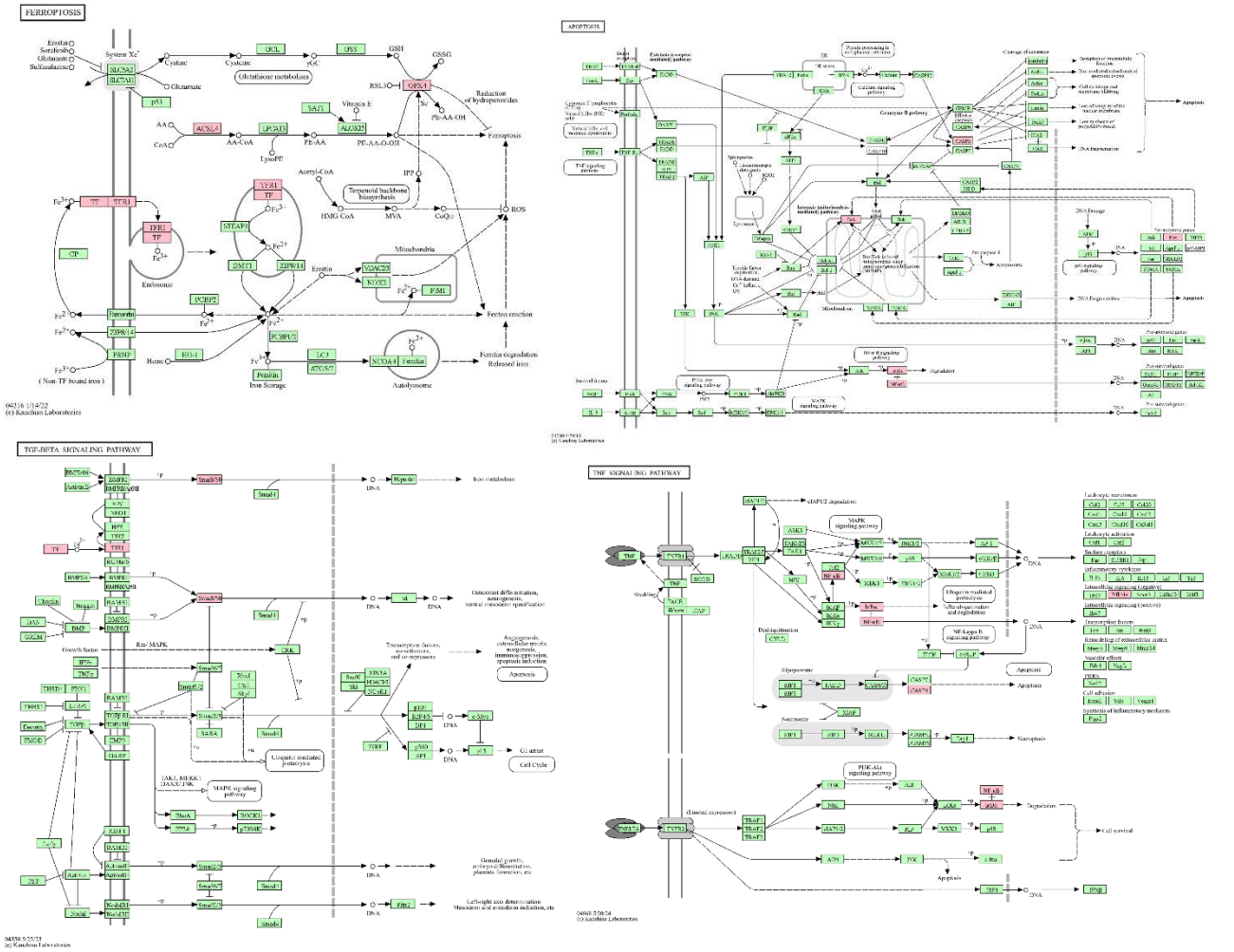

Figure 7. Signaling pathways related to ferroptosis and apoptosis. (modified from KEGG pathway mmu04216, mmu04210, mmu04350 and mmu04668[22])

To further analyze ferroptosis-dominant cell populations, TOGGLE was applied to Groups R2-2 and R2-3, and five groups (Figure 8A). Using the FindAllMarkers function of Seurat, genes uniquely and highly expressed in each group were identified with selection criteria of Log2FC ≥ 0.25 and FDR < 0.05. Ferroptosis driver genes were sourced from the FerrDb database (Ver. 2, http://www.zhounan.org/ferrdb/current/). Among the differentially expressed genes in Groups R3-4 and R3-5, ferroptosis driver and other programmed cell death genes were most prevalent. Furthermore, these groups displayed a higher number of highly expressed ferroptosis driver genes (Log2FC ≥ 2 and FDR < 0.05) compared to other groups, with over 70% of cells in Groups R3-4 and R3-5 showing ferroptosis markers relative to healthy cells (Figure 8B, 8C and 8D). The enrichment results showed that the pathways enriched by differentially expressed genes included ferroptosis (Figure 8E). These findings support identifying Groups R3-4 and R3-5 as ferroptosis-dominant cell populations.

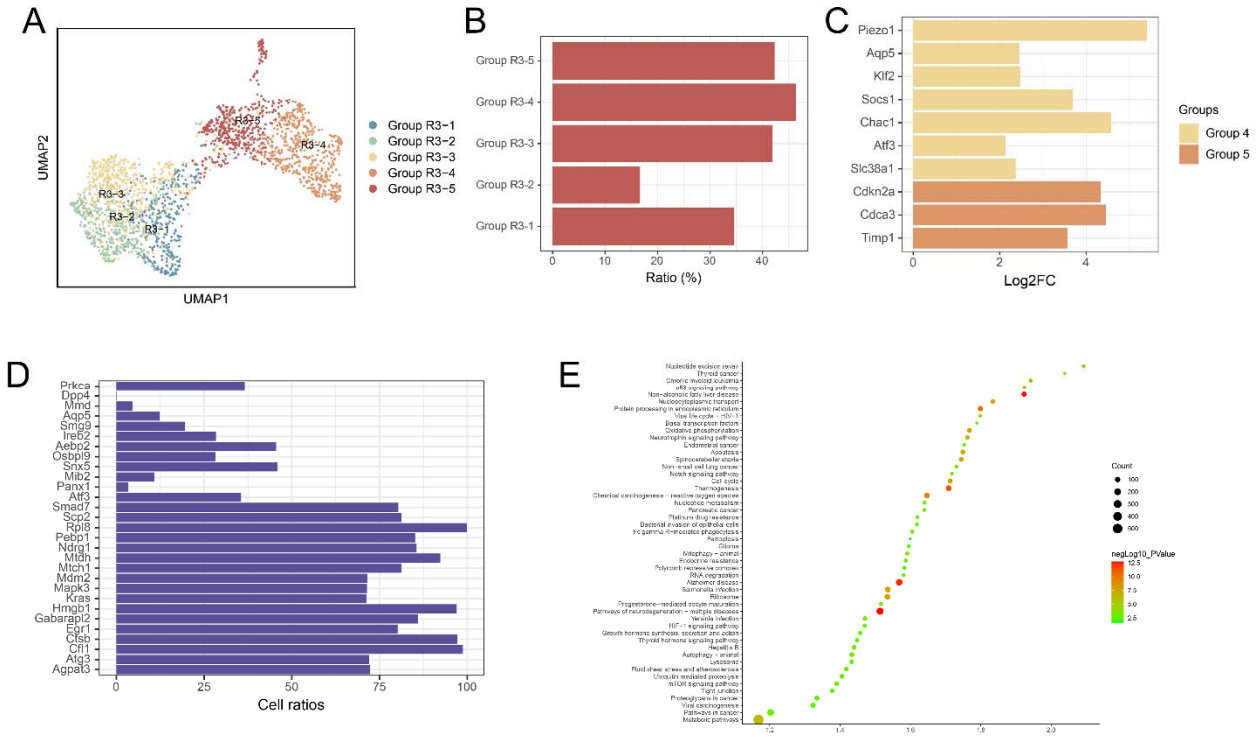

Figure 8. Ferroptotic Neurons Prediction. A: Cells in previous Groups R2-2 and R2-3 further analyzed by TOGGLE and divided into 5 groups; B: The proportion of ferroptosis-driving genes in each cell group; C: Log2FC values of highly expressed ferroptosis-driving genes; D: The proportion of cells expressing different ferroptosis-driving genes; E: Top 50 pathways of Group R3-4 and Group R3-5 genes

2.5 Verification of apoptosis- and ferroptosis-related genes

Our previous research demonstrated increased iron levels and neuronal iron accumulation in the infarcted brain tissue of the MCAO model. Deferiprone treatment in MCAO model effectively reduces iron content and diminishes iron accumulation[23]. Based on these findings, we used the MCAO model ± deferiprone to validate the predicted results of neuronal ferroptosis.

2.5.1 Pathological changes of brain tissue

In the Sham operation group, neurons exhibited normal morphology, with orderly arrangement, clear nuclear membranes, uniformly stained cytoplasm, and no evident pathological changes. In contrast, the MCAO group showed significant structural damage in the ischemic cortical area, with disorganized neuronal arrangement, widened intercellular spaces, and signs of cell swelling, rupture, and nuclear condensation, leading to vacuole formation. In the MCAO+deferiprone group, neuronal structural damage was mild, with minimal cell membrane rupture, slight nuclear condensation, and a significant reduction in vacuolar degeneration (Figure 9).

Figure 9 Pathological changes of brain tissue (HE staining, 40× magnification)

2.5.2 Ultrastructural changes of brain tissue

In the Sham group, mitochondria appeared structurally normal with clear features and intact membranes. In contrast, the MCAO group exhibited mitochondrial atrophy, reduced cristae, and increased membrane density, consistent with the morphological characteristics of ferroptosis. The MCAO+deferiprone group showed significant improvement in mitochondrial integrity compared to the MCAO group, with reduced damage (Figure 10).

Figure 10 Ultrastructural changes of brain tissue (Transmission electron microscope. The upper images are at 1500× magnification, and the lower images are at 6000× magnification. Mitochondria are marked by white arrows.).

2.5.3 Expression levels of *Acsl4, Gpx4* and *Fsp1* proteins detected by immunohistochemistry

Compared to the Sham operation group, the MCAO group showed an increase in Acsl4 levels ($P<0.05$) and a decrease in Gpx4 levels ($P<0.05$). These findings are consistent with the differential gene expression results from single-cell sequencing. Meanwhile, compared to the Sham operation group, the MCAO group showed an decrease in Fsp1 levels ($P<0.05$). Compared with the MCAO group, the MCAO+deferiprone group showed a decrease in Acsl4 levels and Fsp1 levels ($P<0.05$), and a increase in Gpx4 levels ($P<0.05$). (Figure 11).

Figure 11 Expression levels of Acsl4 and Gpx4 proteins. (Immunohistochemistry, 40× magnification. *compared with the sham group, $P<0.05$; #compared with MCAO group, #$P<0.05$. n=3 per group)

2.5.4 Expression levels of *Bax, IkBa, Casp3, p-Smad, p65(Rela), Tfrc, Trf and Sirt1* proteins detected by immunofluorescence staining

Compared to the Sham operation group, the MCAO group exhibited significantly elevated levels of Bax, IκBα, p-Smad, p65 (Rela), Tfrc, and Trf proteins ($P<0.05$). These results are consistent with the differential gene expression findings from the single-cell sequencing analysis. Meanwhile, Compared to the Sham operation group, the Casp3 protein level was increased, while the Sirt1 protein level was decreased in the MCAO group ($P<0.05$) (Figure 12).

Figure 12 Expression levels of Bax, IkBa, p-Smad, p65, Tfrc, and Trf proteins (Immunofluorescence, 40× magnification. Compared with the sham group, *$P<0.05$. n=3 per group).

3 Discussion

This research developed TOGGLE, a unsupervised learning method for predicting cell fate using scRNAseq data. TOGGLE allows researchers to obtain a graph distance matrix between cells, which can be interpreted as a measure of cell similarity. This matrix reveals the approximate relationships between cells. One of the key features of TOGGLE is its flexible method for calculating the similarity matrix. This flexibility allows for easy updates to the algorithm to meet specific requirements, without the need for extensive modifications to subsequent steps. As a result, the scalability of the TOGGLE model is enhanced. Once the similarity matrix is obtained, TOGGLE facilitates the unsupervised clustering of cells, grouping them based on their states. The algorithm's resolution can be adjusted during this step to achieve a desired number of clusters, tailored to the specific needs of the analysis. Cells that are clustered together not only share significant similarity in terms of cell type, but also likely have consistent fate determinations. This ensures their coherence in pseudotemporal order. After determining the cell clusters, TOGGLE can be further utilized to acquire pseudotime ordering results, which enables the reconstruction of the complete dynamical process of the cells.

We established a lineage tracing model using the development and differentiation of hematopoietic stem cells and then utilized reprogrammed cells to construct the lineage of regenerative processes to demonstrate TOGGLE’s utility in elucidating the single-cell functions of forward differentiation and reverse differentiation. We conducted a benchmark evaluation of TOGGLE using two scRNA-seq datasets that include known lineage information. In addition, we constructed an RNA functional map using bulk RNA-seq of the effects of e-cigarette on the myocardium, and constructed a fibroblast functional map and an MI cohort fibroblast RNA functional map using snRNA-seq data of MI, further expanding the application scope of TOGGLE. In this evaluation, we compared the performance of TOGGLE with widely used algorithms. The results reveal that TOGGLE consistently outperformed both WOT and cospar in accurately predicting the fate of progenitor cells and effectively constructing the cell development process through pseudotime calculation. Compared with mainstream algorithms, our method demonstrates the following advancements:

In previous multimodal research, it is typically necessary to first perform non-one-hot encoding on the expression data of a single type, followed by employing optimal transport optimization theory to process these combined expression data. This aligns with the type of data TOGGLE is capable of handling, thus TOGGLE can also be applied within various multimodal models. This application is able to enhance the accuracy of non-one-hot encoding and optimize the optimal transport results of combined data, thereby facilitating multimodal cell fate prediction[30].

The limitations of this study: When the expected number of categories has already been estimated, the desired number of categories can be obtained by adjusting the target number of categories. While the algorithm can automatically identify and provide the estimated number of categories and can reduce resolution to produce more category results, it cannot independently verify the actual number of true categories. Further comparison and calculation of differential genes are required for validation.

4.7 Experimental Materials and Methods

4.7.1 Experimental Materials

(1) Experimental Animal

Fifty male specific pathogen free Sprague-Dawley (SD) rats, aged 6 to 8 weeks and weighing 250-280 g, were provided by the Experimental Animal Center of Hunan University of Chinese Medicine (Animal Quality Certificate No.: 430727211100405318). The rats were purchased from Hunan Sileike Jingda Experimental Animal Co., Ltd. [License No.: SCXK (Xiang) 2019-0004]. They were housed in the Experimental Animal Center of Hunan University of Chinese Medicine [License No.: SYXK (Xiang) 2019-0009] under standard conditions, with a room temperature of (24±1)°C, humidity of approximately 55%, and a 12-hour light/dark cycle. After a one-week acclimation period, the animals were used for the experiments. All animals' care and experimental procedures were approved by the Animal Ethics Committee of Hunan University of Chinese Medicine (Approve number: LL2019092009) and were in accordance with the National Institute of Health's Guide for the Care and Use of Laboratory Animals.

(2) Reagents

Paraformaldehyde (Batch No.: G1101) was purchased from Servicebio, and anhydrous ethanol (Batch No.: 10009259) from China National Pharmaceutical Group Chemical Reagent Co., Ltd. Electron microscopy fixative (Cat. No. G1102) was purchased from Wuhan Guge Biotechnology Co., Ltd. Transferrin (Trf) polyclonal antibody (Cat. No.: 17435-1-AP), Bax polyclonal antibody (Cat. No.: 50599-2-Ig) and IκBα polyclonal antibody (Cat. No.: 10268-1-AP) were obtained from Proteintech. Casp-3 antibody (Cat. No.: 9661L) was purchased from Cell Signaling. Sirt1 antibody (Cat. No. ab189494) was purchased from Abcam. Transferrin receptor (Tfrc) polyclonal antibody (Cat. No.: A5865), and Rela (p65) polyclonal antibody (Cat. No.: A2547) were sourced from ABclonal. P-smad (Cat. No.: AF8313) was acquired from Affinity Bioscience. Gpx4 antibody (Cat. No.: AF301385), Acsl4 polyclonal antibody (Cat. No.: AFW6826) and Fsp1 polyclonal antibody (Cat. No.: AFW21808) were purchased from AiFangbio. DAPI (Cat. No.: ab228549) was obtained from Abcam. Deferiprone tablets (specification: 50 mg/tablet, batch number: H20140379) was purchased form Apotex Inc.

(3) Instruments

The optical microscope (Axioscope-5) was purchased from Zeiss, Germany. The pathology microtome (RM2016) and Leica blades (LEICA-819) were both obtained from Leica Instruments Co., Ltd. The optical microscope (Axioscope-5) was purchased from Zeiss Inc. The pathology microtome (RM2016) and Leica blades (LEICA-819) were purchased from Leica Instruments Shanghai Co., Ltd. Transmission electron microscope (HT7700) was purchased from Hitachi Inc.

4.7.2 Animal Grouping, Modeling and Intervention

Fifty SD rats were randomly assigned into three groups: the Sham operation group, the MCAO group and the MCAO+Deferiprone group, with five rats in each group. The MCAO model was established using a modified reversible middle cerebral artery suture method[37] for the rats in the MCAO group and the MCAO+Deferiprone group. Rats were fasted for 12 hours prior to surgery. During surgery, the right common carotid artery and external carotid artery were exposed and clamped, and a suture was inserted into the internal carotid artery via the common carotid artery to block the origin of the right middle cerebral artery. The suture was advanced approximately 18.5±0.5 mm until resistance was felt, indicating the correct position. The suture was then fixed to both the common and internal carotid arteries, and the incision was closed. Throughout the procedure, care was taken to maintain body temperature, and after surgery, the animals were returned to normal feeding conditions. In the Sham group, no suture was inserted, and the animals were kept under normal conditions.

Successful model establishment was confirmed when the rats exhibited left-sided limb paralysis, instability when standing, or circling behavior when lifted by the tail. Neurological function was scored on a scale of 1 to 3, with non-successful models excluded. The neurological scoring system was based on the Zea Longa scale[37] as shown in Table S3.

Deferiprone tablets were dissolved in a 0.9% sodium chloride solution. Following model establishment, rats in the deferiprone group received oral administration of deferiprone at a dose of 125 mg/kg per day. Rats in the sham operation group and the MCAO group were given an equivalent volume of 0.9% sodium chloride solution. Treatments were administered once daily for three consecutive days.

4.7.3 Neuronal morphological changes observation by hematoxylin-eosin (HE) staining

The brain tissue was perfused with pre-cooled 0.9% sodium chloride solution, followed by fixation in 4% paraformaldehyde at 4°C. The tissue was then coronally sectioned into 4 μm thick slices. The sections were deparaffinized, rehydrated, and stained with hematoxylin for 5 minutes. After differentiation and rinsing with water, the sections were blued with distilled water, dehydrated through a graded ethanol series, and counterstained with eosin for 5 minutes. Following dehydration with ethanol

and clearing with xylene, coverslips were applied and sealed with neutral balsam. Morphological observations and image acquisition were performed under a light microscope.

4.7.4 Transmission electron microscopy

The affected brain tissue was sectioned into 1 mm-thick slices. Samples were immersed in electron microscopy fixative at 4°C overnight, followed by fixation in 1% osmium tetroxide at 4°C for 2 hours. The samples were stained with 1% uranyl acetate for 1 hour, dehydrated, and embedded in epoxy resin. Ultrathin sections were prepared using an ultramicrotome, stained with uranyl acetate and lead citrate, and examined under a transmission electron microscope.

4.7.5 Immunohistochemical Staining for Acsl4, Gpx4 and Fsp1 Protein Expression Levels

Paraffin-embedded tissue sections (5 μm) were deparaffinized and rehydrated. Endogenous enzymes were inactivated by incubating the sections in 3% hydrogen peroxide at room temperature for 10 minutes, followed by two washes with distilled water. Antigen retrieval was performed by immersing the sections in 0.01 mol/L citrate buffer (pH 6.0) and heating in a microwave until boiling, then turning off the power and repeating the process after a 5-minute interval. After cooling, the sections were washed twice with PBS buffer (pH 7.2-7.6) for 3 minutes each. Blocking solution was added and incubated at room temperature for 20 minutes, with excess liquid removed without washing. Primary antibodies were applied and incubated at 37°C for 2 hours, followed by three washes with PBS buffer (pH 7.2-7.6) for 3 minutes each. Biotinylated secondary antibody solution was added and incubated at 20-37°C for 20 minutes, followed by another round of PBS washing. Streptavidin-HRP was applied and incubated at 20-37°C for 20 minutes, followed by washing in PBS as described earlier. DAB was used for color development, with reaction time controlled under a microscope (5-30 minutes). Sections were lightly counterstained with hematoxylin, dehydrated, cleared, and mounted with neutral balsam for microscopic observation of Acsl4 and Gpx4 protein expression. Images from five randomly selected fields of view from different samples were captured, and average optical density was analyzed using ImageJ software.

4.7.6 Immunofluorescence Staining for Bax, IκBα, Casp3, p-Smad, p65 (Rela), Tfrc, Trf, and Sirt1 Protein Expression Levels

Paraffin sections were deparaffinized and rehydrated, followed by membrane permeabilization with 0.3% Triton X-100 for 5 minutes. The sections were then blocked with 5% BSA in PBST at room temperature for 1 hour. Primary antibodies, diluted in PBST, were applied, and the sections were incubated overnight at 4°C. After washing with PBST, fluorescent secondary antibodies were added, and the sections were incubated in the dark at room temperature for 1 hour. The secondary antibodies were washed off, and the slides were mounted with anti-fade mounting medium containing DAPI. The next

day, images were captured using a panoramic tissue cell quantification system at 40x magnification. Images from five randomly selected fields of view from different samples were captured and analyzed using ImageJ software to assess the average fluorescence intensity.

4.8 Statistical Analysis

All data are presented as Mean±SD, and statistical analysis and graphing were performed using GraphPad Prism 9.0. Non-parametric tests were used to analyze average fluorescence intensity and average optical density. A P-value of less than 0.05 was considered statistically significant.

Code and Data availability

Contribution

The methodology, bioanalysis, and test application of this paper were collaboratively designed by Junpeng Chen*+, Eric Jiang+, Zhouweiyu Chen+, and Kailin Yang+*. Through long-term alterations in RNA pathways, cells may ultimately change their function. Junpeng Chen organized and led the entire study, defining the manuscript's topic and narrative. Junpeng Chen, Zhouweiyu Chen and Yuwei Li were the main contributors to the algorithm innovation, while Junyao Jiang and Kailin Yang were the main contributors to the bioanalysis and bio-innovation. Zhouweiyu Chen assisted in solving critical computational problems, and Yuwei Li completed the design and testing of auxiliary plans, making the method complete. Junyao Jiang proposed a complete set of biological problems and performed the analysis, with assistance from Junpeng Chen and Kailin Yang. The entire paper was reviewed by Yunhui Kong with exceptional scholarship, who offered constructive modifications. Alex P. Carll played a crucial role in correspondence, providing experimental resources and research funding. Junpeng Chen, Alex P. Carll, and Lu Cai jointly organized the study. Alex P. Carll, Yibing Nong guided the analysis of cardiac pathway differences and cardiomyocytes. Lu Cai supervised the experimental work on ferroptosis. Richa A. Singhal : Contributed critical insights into methodolgy, assisted in revisions, and supported manuscript writing and refinement.

Acknowledgments

"***This research was supported in part by the U.S. National Science Foundation*** (***NSF***) ***under grant CNS***1828521 ***and the University of Louisville's Research Computing team***." *The University of Louisville provided computational equipment support for this research and assisted all researchers with equipment maintenance and update. These*

hardworking and dedicated staff members share this honor with us, including the following staff: ***Harrison Simrall***, ***Tomas Felipe Llano Rios***, and ***Randy Vargas***.

References

---

1. Galluzzi, L., Vitale, I., Aaronson, S. A., Abrams, J. M., Adam, D., Agostinis, P., Alnemri, E. S., Altucci, L., Amelio, I., Andrews, D. W. et al, Zitvogel, L., Melino, G. & Kroemer, G. Molecular mechanisms of cell death: recommendations of the Nomenclature Committee on Cell Death 2018. *Cell Death Differ* **25,** 486–541 (2018).
2. Moujalled, D., Strasser, A. & Liddell, J. R. Molecular mechanisms of cell death in neurological diseases. *Cell Death Differ* **28,** 2029–2044 (2021).
3. Qin, H., Abulaiti, A., Maimaiti, A., Abulaiti, Z., Fan, G., Aili, Y., Ji, W., Wang, Z. & Wang, Y. Integrated machine learning survival framework develops a prognostic model based on inter-crosstalk definition of mitochondrial function and cell death patterns in a large multicenter cohort for lower-grade glioma. *Journal of Translational Medicine* **21,** 588 (2023).
4. Zhang, Q., Jia, M., Wang, Y., Wang, Q. & Wu, J. Cell Death Mechanisms in Cerebral Ischemia–Reperfusion Injury. *Neurochem Res* **47,** 3525–3542 (2022).
5. Wang, X., Chen, X., Zhou, W., Men, H., Bao, T., Sun, Y., Wang, Q., Tan, Y., Keller, B. B., Tong, Q., Zheng, Y. & Cai, L. Ferroptosis is essential for diabetic cardiomyopathy and is prevented by sulforaphane via AMPK/NRF2 pathways. *Acta Pharm Sin B* **12,** 708–722 (2022).
6. Zeng, L., Yang, K., Yu, G., Hao, W., Zhu, X., Ge, A., Chen, J. & Sun, L. Advances in research on immunocyte iron metabolism, ferroptosis, and their regulatory roles in autoimmune and autoinflammatory diseases. *Cell Death Dis* **15,** 481 (2024).
7. Liao, M., Qin, R., Huang, W., Zhu, H.-P., Peng, F., Han, B. & Liu, B. Targeting regulated cell death (RCD) with small-molecule compounds in triple-negative breast cancer: a revisited perspective from molecular mechanisms to targeted therapies. *J Hematol Oncol* **15,** 44 (2022).
8. Qin, R., You, F.-M., Zhao, Q., Xie, X., Peng, C., Zhan, G. & Han, B. Naturally derived indole alkaloids targeting regulated cell death (RCD) for cancer therapy: from molecular mechanisms to potential therapeutic targets. *J Hematol Oncol* **15,** 133 (2022).
9. Weinreb, C., Rodriguez-Fraticelli, A., Camargo, F. D. & Klein, A. M. Lineage tracing on transcriptional landscapes links state to fate during differentiation. *Science* **367,** eaaw3381 (2020).
10. Moreno-Ayala, R. & Junker, J. P. Single-cell genomics to study developmental cell fate decisions in zebrafish. *Brief Funct Genomics* elab018 (2021). doi:10.1093/bfgp/elab018
11. Ma, H., Zhou, Y., Li, Z., Zhu, L., Li, H., Zhang, G., Wang, J., Gong, H., Xu, D., Hua, W., Liu, P., Zhang, X., Zhang, Y., Zhang, L., Hong, B., Zhou, W., Yang, P. & Liu, J. Single-Cell RNA-Sequencing Analyses Revealed Heterogeneity and Dynamic Changes of Metabolic Pathways in Astrocytes at the Acute Phase of Ischemic Stroke. *Oxid Med Cell Longev* **2022,** 1817721 (2022).
12. Liu, T., Bai, M., Liu, M., Li, T., Liao, Y., Zhao, C., Yao, M., Wang, J., Wen, A. & Ding, Y. Novel synergistic mechanism of 11-keto-β-boswellic acid and Z-Guggulsterone on ischemic stroke revealed by single-cell transcriptomics. *Pharmacol Res* **193,** 106803 (2023).
13. Nakamura, A., Sakai, S., Taketomi, Y., Tsuyama, J., Miki, Y., Hara, Y., Arai, N., Sugiura, Y., Kawaji, H., Murakami, M. & Shichita, T. PLA2G2E-mediated lipid metabolism triggers brain-autonomous neural repair after ischemic stroke. *Neuron* **111,** 2995-3010.e9 (2023).
14. Schiebinger, G., Shu, J., Tabaka, M., Cleary, B., Subramanian, V., Solomon, A., Gould, J., Liu, S., Lin, S., Berube, P., Lee, L., Chen, J., Brumbaugh, J., Rigollet, P., Hochedlinger, K., Jaenisch, R., Regev,

A. & Lander, E. S. Optimal-Transport Analysis of Single-Cell Gene Expression Identifies Developmental Trajectories in Reprogramming. *Cell* **176,** 928-943.e22 (2019).
15. Wang, S.-W., Herriges, M. J., Hurley, K., Kotton, D. N. & Klein, A. M. CoSpar identifies early cell fate biases from single-cell transcriptomic and lineage information. *Nat Biotechnol* **40,** 1066–1074 (2022).
16. Obeng, E. Apoptosis (programmed cell death) and its signals - A review. *Braz. J. Biol.* **81,** 1133–1143 (2021).
17. Bedoui, S., Herold, M. J. & Strasser, A. Emerging connectivity of programmed cell death pathways and its physiological implications. *Nat Rev Mol Cell Biol* **21,** 678–695 (2020).
18. Tuo, Q., Zhang, S. & Lei, P. Mechanisms of neuronal cell death in ischemic stroke and their therapeutic implications. *Medicinal Research Reviews* **42,** 259–305 (2022).
19. Biddy, B. A., Kong, W., Kamimoto, K., Guo, C., Waye, S. E., Sun, T. & Morris, S. A. Single-cell mapping of lineage and identity in direct reprogramming. *Nature* **564,** 219–224 (2018).
20. Neczypor, E. W., Saldaña, T. A., Mears, M. J., Aslaner, D. M., Escobar, Y.-N. H., Gorr, M. W. & Wold, L. E. e-Cigarette Aerosol Reduces Left Ventricular Function in Adolescent Mice. *Circulation* **145,** 868–870 (2022).
21. Zhou, N., Yuan, X., Du, Q., Zhang, Z., Shi, X., Bao, J., Ning, Y. & Peng, L. FerrDb V2: update of the manually curated database of ferroptosis regulators and ferroptosis-disease associations. *Nucleic Acids Research* **51,** D571–D582 (2023).
22. Kanehisa, M., Sato, Y. & Kawashima, M. KEGG mapping tools for uncovering hidden features in biological data. *Protein Sci* **31,** 47–53 (2022).
23. Lan, B., Ge, J.-W., Cheng, S.-W., Zheng, X.-L., Liao, J., He, C., Rao, Z.-Q. & Wang, G.-Z. Extract of Naotaifang, a compound Chinese herbal medicine, protects neuron ferroptosis induced by acute cerebral ischemia in rats. *J Integr Med* **18,** 344–350 (2020).
24. Shi, H., Song, L., Wu, Y., Shen, R., Zhang, C., Liao, X., Wang, Q. & Zhu, J. Edaravone Alleviates Traumatic Brain Injury by Inhibition of Ferroptosis via FSP1 Pathway. *Mol Neurobiol* (2024). doi:10.1007/s12035-024-04216-2
25. Wang, X., Shao, N., Zhang, X., Chen, H., Chang, Z., Xie, D. & Zhang, J. Ferulic Acid Activates SIRT1-Mediated Ferroptosis Signaling Pathway to Improve Cognition Dysfunction in Wilson's Disease. *Neuropsychiatric Disease and Treatment* **19,** 2681–2696 (2023).
26. Liu, G., Wang, T., Wang, T., Song, J. & Zhou, Z. Effects of apoptosis□related proteins caspase□3, Bax and Bcl□2 on cerebral ischemia rats. *Biomedical Reports* **1,** 861–867 (2013).
27. Zhou, Y., Liao, J., Mei, Z., Liu, X. & Ge, J. Insight into Crosstalk between Ferroptosis and Necroptosis: Novel Therapeutics in Ischemic Stroke. *Oxidative Medicine and Cellular Longevity* **2021,** 9991001 (2021).
28. Yang, K., Zeng, L., Yuan, X., Wang, S., Ge, A., Xu, H., Zeng, J. & Ge, J. The mechanism of ferroptosis regulating oxidative stress in ischemic stroke and the regulation mechanism of natural pharmacological active components. *Biomedicine & Pharmacotherapy* **154,** 113611 (2022).
29. Jindal, K., Adil, M. T., Yamaguchi, N., Yang, X., Wang, H. C., Kamimoto, K., Rivera-Gonzalez, G. C. & Morris, S. A. Single-cell lineage capture across genomic modalities with CellTag-multi reveals fate-specific gene regulatory changes. *Nat Biotechnol* **42,** 946–959 (2024).
30. Sha, Y., Qiu, Y., Zhou, P. & Nie, Q. Reconstructing growth and dynamic trajectories from single-cell transcriptomics data. *Nat Mach Intell* **6,** 25–39 (2023).
31. Wang, B., Zhu, J., Pierson, E., Ramazzotti, D. & Batzoglou, S. Visualization and analysis of single-cell RNA-seq data by kernel-based similarity learning. *Nat Methods* **14,** 414–416 (2017).
32. Jiang, J., Ye, X., Kong, Y., Guo, C., Zhang, M., Cao, F., Zhang, Y. & Pei, W. scLTdb: a comprehensive single-cell lineage tracing database. *Nucleic Acids Research* gkae913 (2024). doi:10.1093/nar/gkae913

33. Jiang, J., Li, J., Huang, S., Jiang, F., Liang, Y., Xu, X. & Wang, J. CACIMAR: cross-species analysis of cell identities, markers, regulations, and interactions using single-cell RNA sequencing data. *Briefings in Bioinformatics* **25,** bbae283 (2024).
34. Jiang, J., Lyu, P., Li, J., Huang, S., Tao, J., Blackshaw, S., Qian, J. & Wang, J. IReNA: Integrated regulatory network analysis of single-cell transcriptomes and chromatin accessibility profiles. *iScience* **25,** 105359 (2022).
35. Kong, Y., Jiang, J., Kong, W. & Qin, S. DRCTdb: disease-related cell type analysis to decode cell type effect and underlying regulatory mechanisms. *Commun Biol* **7,** 1205 (2024).
36. Jin, S., Plikus, M. V. & Nie, Q. CellChat for systematic analysis of cell–cell communication from single-cell transcriptomics. *Nat Protoc* (2024). doi:10.1038/s41596-024-01045-4
37. Longa, E. Z., Weinstein, P. R., Carlson, S. & Cummins, R. Reversible middle cerebral artery occlusion without craniectomy in rats. *Stroke* **20,** 84–91 (1989).
38. Lange, M., Bergen, V., Klein, M. et al. CellRank for directed single-cell fate mapping. Nat Methods 19, 159–170 (2022).
39. Bannon, D., Moen, E., Schwartz, M. et al. DeepCell Kiosk: scaling deep learning–enabled cellular image analysis with Kubernetes. Nat Methods 18, 43–45 (2021).
40. Lotfollahi, M., Wolf, F.A. & Theis, F.J. scGen predicts single-cell perturbation responses. Nat Methods 16, 715–721 (2019).
41. C. Domínguez Conde et al. ,Cross-tissue immune cell analysis reveals tissue-specific features in humans.Science376,eabl5197(2022).
42. Aibar, S., González-Blas, C., Moerman, T. et al. SCENIC: single-cell regulatory network inference and clustering. Nat Methods 14, 1083–1086 (2017).
43. Van de Sande, B., Flerin, C., Davie, K. et al. A scalable SCENIC workflow for single-cell gene regulatory network analysis. Nat Protoc 15, 2247–2276 (2020).
44. Schiebinger, Geoffrey, et al. "Optimal-transport analysis of single-cell gene expression identifies developmental trajectories in reprogramming." Cell 176.4 (2019): 928-943.
45. Chu, B.K., Tse, M.J., Sato, R.R. et al. Markov State Models of gene regulatory networks. BMC Syst Biol 11, 14 (2017).
46. Wang, SW., Herriges, M.J., Hurley, K. et al. CoSpar identifies early cell fate biases from single-cell transcriptomic and lineage information. Nat Biotechnol 40, 1066–1074 (2022).